BBA - General Subjects 1863 (2019) 502–510

Contents lists available at ScienceDirect

BBA - General Subjects

journal homepage: www.elsevier.com/locate/bbagen

Missing-in-metastasis protein promotes internalization of magnetic nanoparticles *via* association with clathrin light chain and Rab7

Peng Zhao[a,b], Bo Chen[a,e], Lushen Li[c], Hao Wu[d], Yan Li[a,b], Baxter Shaneen[c], Xi Zhan[c,*], Ning Gu[a,b,*]

[a] State Key Laboratory of Bioelectronics, Jiangsu Key Laboratory for Biomaterials and Devices, School of Biological Science and Medical Engineering, Southeast University, Nanjing 210096, PR China
[b] Collaborative Innovation Center of Suzhou Nano Science and Technology, Suzhou 215123, PR China
[c] Center for Vascular and Inflammatory Diseases, University of Maryland School of Medicine, Baltimore, MD 21201, USA
[d] School of Biomedical Engineering and Informatics, Nanjing Medical University, Nanjing 210029, PR China
[e] Materials Science and Devices Institute, Suzhou University of Science and Technology, 1 Kerui Road, Suzhou, Jiangsu 215009, PR China

ARTICLE INFO

Keywords:
MIM
Magnetic nanoparticles
Endocytosis
Clathrin
Rab7

ABSTRACT

Background: Magnetic nanoparticles (MNPs) have been widely used in biomedical applications. Proper control of the duration of MNPs in circulation promises to improve further their applications, in particularly drug delivery. It is known that the uptake of tissue-associated MNPs is mainly carried out by macrophages. Yet, the molecular mechanism to control MNPs internalization in macrophages remains to be elusive. Missing-in-metastasis (MIM) is a scaffolding protein that is highly expressed in macrophages and regulates receptor-mediated endocytosis. We hypothesize that uptake of MNPs may also involve the function of MIM.

Methods: We investigated the effect of MIM expression on the intracellular trafficking of MNPs by transmission electronic microscopy, flow cytometry, o-phenanthroline photometric analysis, Perl's staining, immunofluorescence microscopy and co-immunoprecipitation. To explore the molecular events in MIM-mediated MNPs uptake, we examined the effect of MNPs on the interaction of MIM with clathrin, Rab5 and Rab7.

Results: Uptake of MNPs was significantly enhanced in cells overexpressing MIM. Upon exposure to MNPs, MIM was associated with clathrin light chain in endocytic vesicles and Rab7, a protein that regulates late endosomes. However, MNPs caused dissociation of MIM with Rab5, an early endosome-associated protein.

Conclusions: MIM regulates internalization of MNPs *via* promoting their trafficking from plasma membrane to late endosomes.

General significance: Our data unveiled a novel pathway which MNPs internalization and intracellular trafficking in macrophages. This new pathway may allow us to control the uptake of MNPs within cells by targeting MIM, thereby improving their medical applications.

1. Introduction

Magnetic nanoparticles (MNPs) possess unique physical and chemical properties [1] and have been extensively used in a variety of biomedical applications, including magnetic resonance imaging [2], heating mediators for hyperthermia [3], cell labeling and tracking [4], cell sensing [5], drug delivery [6] and theragnostics [7]. Many of these applications require the injection of nanomaterials into the blood circulation, and the success of their usages depends largely on the duration of the particles once internalized into targeted cells. Yet, the clearance profile of these nanomaterials within cells is unknown [8]. After entering tissues through the bloodstream, nanoparticles tend to complex with certain serum proteins, which forms a “corona” that influences greatly the biological property of the particles [9–11]. These serum proteins act as opsonin and facilitate the uptake of nanoparticles by the mononuclear phagocyte system (MPS), which is regarded as a limit step for long-circulating and targeting [12–14]. Therefore, minimizing the clearance of MPS, especially by macrophages, would likely increase their duration *in vivo*, thereby improving the efficacy of their applications [15,16].

A few endocytic pathways have been implicated in the uptake of nanoparticles into cells [17]. These include, but not limited to, clathrin/

* Corresponding authors at: State Key Laboratory of Bioelectronics, Jiangsu Key Laboratory for Biomaterials and Devices, School of Biological Science and Medical Engineering, Southeast University, Nanjing 210096, PR China.
E-mail addresses: xzhan@som.umaryland.edu (X. Zhan), guning@seu.edu.cn (N. Gu).

https://doi.org/10.1016/j.bbagen.2018.12.002
Received 30 September 2018; Received in revised form 5 November 2018; Accepted 4 December 2018
Available online 06 December 2018

caveolae-mediated endocytosis, phagocytosis, macropinocytosis and pinocytosis. Among them, the clathrin-mediated endocytosis is considered as the major route for MNPs to be internalized into macrophages [18]. The entire process of clathrin-mediated endocytosis involves extensive membrane deformations, which are initiated by a series of membrane sculfing proteins. Many of these proteins belong to the Bin/amphiphysin/Rvs (BAR) domain superfamily, which includes several subfamilies, including BAR/N-BAR, EFC/F-BAR and I-BAR domain proteins [19]. These BAR domain proteins sense and generate membrane curvatures by binding or insertion into specific phospholipid membranes through a curved interface organized by their BAR domains [20]. BAR domain proteins that have been involved in the clathrin-mediated endocytosis include endophilin, amphiphysin, SNX9, FBP17 and syndapin [21]. In addition, FCHo1/Syp1 F-BAR proteins have also been implicated in the budding of the clathrin-coated pits. During the formation of clathrin-coated pits, amphiphysin and endophilin recruit dynamin to the neck region *via* their SH3 domains [22]. SNX9 contains several binding sites for AP-2 and localizes clathrin subunits to a budding neck, which ensures the generation of clathrin-coated vesicles [21,23].

Unlike traditional BAR domain proteins, the role of I-BAR domain proteins in the clathrin-mediated endocytosis is less understood. A representative of the I-BAR domain protein subfamily is MIM, or metastasis suppressor 1 (MTSS1), which regulates actin dynamics and promotes membrane deformation [19,24]. Although MIM does not have an SH3 domain, it interacts with multiple cellular proteins, including PTPδ, cortactin, Rac and AIP4, and has been involved in filopodia-like protrusive extensions, cell migration, cell-cell interaction and endocytosis [25]. Recent studies have also suggested that MIM participates in the trafficking of internalized cargos within cells [26,27]. However, the role of MIM in endocytosis is uncertain as *drosophila* MIM actually inhibits the endocytosis of EGFR by competing with endophilins [28], indicating that MIM may play different roles in endocytosis in a context-dependent manner.

We have recently observed that mammalian MIM is an effector of Rab GTPases in the endocytosis mediated by chemokine receptor CXCR4 and associated with late endosomes *via* binding to Rab7 [29], a small GTPase that plays a vital role in the maturation of late endosomes from early endosomes. Also, MIM is the only member of the I-BAR domain family that is highly expressed in macrophages [30] and plays a positive role in the internalization of nanoparticles [31]. However, it was unclear about specific process of MNPs in macrophages that is regulated by MIM. In the presented study, we attempted to investigate the MIM-mediated molecular events during the internalization of MNPs in macrophages and found that MNPs triggered the association of MIM with clathrin light chain (CLC) and Rab7. Interestingly, MIM failed to interact with clathrin heavy chain during early responses to MNPs. As both CLC and Rab7 are implicated in sorting of endocytic vesicles, our data suggest that MNPs are processed within macrophages through an intracellular traffic machinery involving the functions of MIM, CLC and Rab7.

2. Materials and methods

2.1. Material and reagents

Lipofectamine 2000 transfection reagent (Cat. No. 11668027), anti-GFP antibody (Cat. No. A11122), FITC-conjugated goat anti-rabbit (Cat. No. A16097), Alexa flour 488-conjugated goat anti-rabbit IgG (Cat. No.A11008), and Alexa flour 568-conjugted goat anti-mouse IgG (Cat. No.A11004) antibodies were purchased from Invitrogen. Antibody against MIM (Cat. No. PA5-17047), Cell Dissociation Buffer (Cat. No. 13151014), protein A/G agarose beads (Cat. No. 20423) and G418 sulfate (Cat. No. 10131035) were purchased from Thermo Scientific. Anti-CD107a (LAMP-1) antibody (Cat. No. sc20011) was purchased from Santa Cruz. Anti-EEA1 (Cat. No. ab70521) and anti-CD63 (Cat. No. ab213090) antibodies were from Abcam. Protease Inhibitor Cocktail (Cat. No. P8340), monoclonal antibodies against clathrin light chain (Cat. No. C1985), clathrin heavy chain (Cat. No. C1860), Rab7 (Cat. No.R8779) and anti-Rab5 (Cat. No. R7904) were purchased from Sigma-Aldrich. Phosphate-Buffered Saline (PBS) (Cat. No. 21–040-CV) was purchased from Corning. Anti-β-actin antibody was from Keygen Biotech. MTT detection kit, RIPA lysis buffer, BCA kit and ECL detection kit were purchased from Beyotime Biotech.

2.2. Synthesis and characterization of ferumoxytol nanoparticles

The iron oxide core of MNPs, which was made of γ-Fe_2O_3, was synthesized by hydrocooling and magnetically internal heating coprecipitation (HMIHC) procedure followed by coating with dextran as described previously [32]. The hysteresis loop of MNPs was measured by vibrating sample magnetometer (LS 7307–9309, Lakeshore Cryotronic, US). The hydrodynamic diameters of MNPs were measured based on dynamic light scattering (DLS) using Zetasizer Nano ZS (Malvern Instruments, UK). To visualize the size and morphology of MNPs, samples were applied to a copper grid, dehydrated and examined by transmission electron microscopy (TEM, JEM-2000EX, JEOL, Japan). The MNPs concentrations were calculated based on the amount of Fe ion, which was measured by ICP-OES (Inductively coupled plasma atomic emission spectroscopy) using Perkin Elmer Optima 2100DV. In brief, the prepared MNPs were incubated with HNO_3 for 16 h to destruct the particles. For ICP-OES analysis, the digested samples were diluted by at least 1:20 folds.

2.3. Cell culture and transfection

RAW 264.7 (RAW) cells (Type Culture Collection of the Chinese Academy of Sciences, Shanghai, China) were maintained in Dulbecco's Modified Eagle's Medium (DMEM) (Invitrogen) supplemented with 10% (*v*/v) fetal bovine serum (HyClone, Thermo Scientific) and 1% penicillin/streptomycin at 37 °C in 5% CO_2 atmosphere. Plasmids encoding MIM-GFP and GFP have been described previously [19,33]. DNA-mediated transfection was performed by using Lipofectamine 2000 Transfection Reagent according to the manufacturer's instruction. Stable transfected cells were selected in the medium containing 0.5 mg/mL G418. The selection medium was replaced every 2–3 days with freshly prepared G418-containing media. Once the stable transfected cells were established, they were maintained in the G418-containing medium.

2.4. Cytotoxicity assay

Cell viability was assessed by using the MTT assay according to the manufacturer's instruction. Briefly, RAW cells were seeded in 96-well plates at a density of 3000 cells per well, cultured overnight and treated with MNPs at the concentrations ranging from 10 μg/mL to 2500 μg/mL. After 24 h of incubation, cells were further treated for 4 h with MTT at a final concentration of 0.5 mg/mL. The resulting formazan crystals were dissolved in 150 μL DMSO and incubated for 10 min at room temperature. The absorbance of samples in each well was measured and recorded by a microplate reader (ELx 800; BioTek, USA) at 490 nm. The spectrophotometer was calibrated to zero absorbance based on wells containing culture medium only. The viability of cell samples was calculated based on the ratio of [T] to [C] × 100, where [T] is the absorbance of the testing sample and [C] is the absorbance of the control sample.

2.5. Cellular uptake of MNPs

Cells were seeded in 6-well plates at a density of 2×10^5 cells/well and cultured overnight. MNPs were added to each well at final iron concentrations ranging from 10 μg/mL to 200 μg/mL. The treated cells

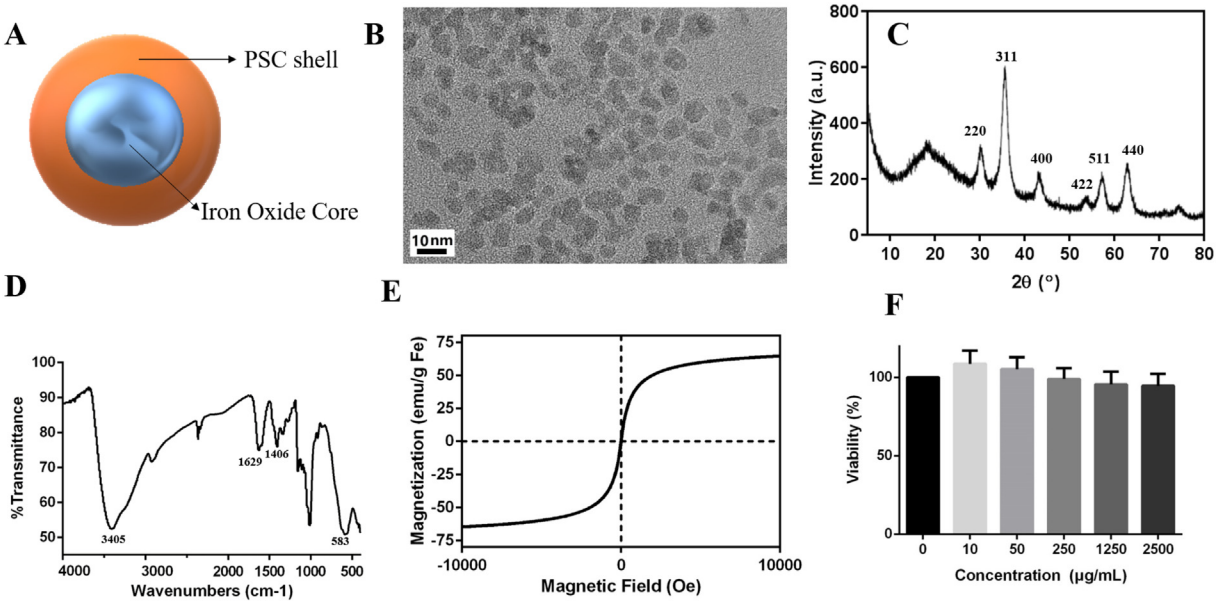

Fig. 1. Characterizations of the physical property of Ferumoxytol MNPs. (A) Schematic presentation of the structure of Ferumoxytol composed of an iron oxide core (Fe_2O_3) (blue) and a PSC shell (orange). (B) TEM analysis of MNPs. A representative TEM image is provided to show the average diameter of MNPs in the range of 6–8 nm. (C) X-ray diffraction analysis of MNPs, which demonstrated that MNPs have a diffraction pattern that matches with that of γ-Fe_2O_3. (D) IR spectrum analysis demonstrated that MNPs have the expected chemical components of PSC-coated Fe_2O_3. (E) Analysis of MNPs by hysteresis loop demonstrated that MNPs have a saturation magnetization (Ms) of 65 emu/g. (F) Analysis of the effect of MNPs on the viability of RAW cells. Cells were treated with MNPs for 24 h at concentrations as indicated and subsequently analyzed by MTT. No statistical difference in cell viability was observed between all treated groups and the untreated group.

were further incubated for additional 24 h prior to analysis of the uptake of MNPs, which was measured either by using o-phenanthroline photometric method [34] or based on side scattering (SSC), a parameter that measures cellular granularity [35]. The brief o-phenanthroline photometric method is the following. The lysates of treated cells were mixed with 6 M hydrochloric acid (HCl) to dissolve the MNPs, followed by incubation 1 h with 10% aqueous solution of hydroxylamine hydrochloride to reduce Fe(III) to Fe(II). The treated samples were further incubated for 1 h at room temperature in ammonium acetate–acetic acid buffer containing 0.1% o-phenanthroline. The formed Fe-phenanthroline complex was evaluated based on the absorbance measured at 510 nm with a spectrophotometer (UV-3600, Shimadzu, Japan). The protein concentration of the lysates samples were determined by BCA assay. The SSC-based assay has been described previously [31]. Briefly, cells were treated with MNPs. After 4 h, cells were collected, washed with PBS three times, and resuspended in 1 mL PBS prior to flow cytometry.

2.6. Immunofluorescence microscopy

Cells were treated with 100 μg/mL MNPs in the growth medium (DMEM + serum). After 4 h, cells were washed with PBS, fixed in 4% formaldehyde in PBS at room temperature for 15 min, and permeabilized with 0.05% saponin for 10 min. The treated cells were blocked by 5% goat serum in PBS then incubated with 100 μL of primary antibody at 5 μg/mL for 1 h at room temperature. After rinsing three times with PBS, the cells were incubated with Alexa-Flour-conjugated secondary antibody for 1 h in dark, washed and mounted. The treated cells were examined under laser scanning confocal microscope (TCS SP8, Leica, Germany).

2.7. Co-immunoprecipitation assay

Co-immunoprecipitation was performed as described previously [29]. Briefly, cells were grown in 10-cm dishes. When cultures reached to 90% confluence, cells were starved in DMEM for 2 h and then treated with 100 μg/mL MNPs in normal growth medium for times up to 240 min. The lysates of treated cells were incubated with 20 μL of 50% (*v*/v) protein-A beads (Invitrogen) for 90 min at 4 °C and centrifuged at 100*g*. The supernatant was mixed with 5 μg/mL anti-MIM (or GFP) antibody, incubated overnight at 4 °C and mixed with 100 μL of protein-A beads. After 2 h of incubation, the mixture was centrifuged at 2000 rpm for 30 s. The pellet was washed three times with 0.5 mL lysis buffer, dissolved in 60 μL SDS sample buffer, boiled for 10 min and subjected to SDS-PAGE followed by Western blot using antibodies against clathrin, Rab5 and Rab7, respectively. Western blot assay was performed as described previously [31].The targeted proteins were detected by enhanced chemiluminescence (ECL). Densitometry analysis of images was performed with Image J software, and results were presented based on three independent experiments.

2.8. Transmission electron microscopy

RAW cells were seeded in a 25 cm^2 flask at the density of 2×10^5 cells/mL and cultured overnight. MNPs were added to a final iron concentration of 100 μg/mL. After 4 h of incubation, the cells were pelleted and washed with PBS, fixed with 2.5% glutaraldehyde for 1 h, and further treated with 1% osmium tetroxide for 1 h. The cell samples were dehydrated in alcohol at a series of concentrations (50%, 70%, 80%, 90%, 95%, and 100% alcohol), and embedded in epoxy resin. The embedded samples were cut into ultrasections of 70 nm with an ultramicrotome. The sample sections were then transferred to a 300-mesh copper grid, stained with 5% uranyl acetate and examined by a transmission electron microscope (TEM, HITACHIH-600) at 80 kV.

2.9. Statistical methodology

All the data were represented as the mean of three to five independent experiments, and error bars are presented as standard deviation (SD). Comparisons were performed using a one-tailed Student's *t*-test (*$P < .05$, ** $P < .01$, *** $P < .001$.).

Table 1
Dynamic scattering analysis of MNPs.

Sample	Hydrodynamicsize (nm)	Polydispersityindex	Zeta potential (mV)	Saturationmagnetization(emu/g)
MNPs	30.15 ± 0.18	0.158 ± 0.016	−28.5 ± 0.4	65 ± 2

3. Results and discussions

3.1. Characterization of Ferumoxytol nanoparticles

Ferumoxytol magnetic nanoparticles (MNPs),which were composed of an iron oxide core and a polyglucose sorbitol carboxymethyether (PSC) shell (Fig. 1A), were prepared as described previously [36]. The physical property of the prepared MNPs was initially examined by TEM, which revealed that most of the particles were quasi-spherical with an average diameter of 7 nm (Fig. 1B). Consistently, the average hydrodynamic size of MNPs was about 30.15 nm with an apparent zeta potential of −28.7 mV as estimated by dynamic light scattering analysis (Table 1). Thus, the prepared nanoparticles have a size range compatible with those that are able to trigger a clathrin-mediated endocytosis [37]. We chose negative charged nanoparticles Ferumoxytol because of their good monodispersity and high stability. When nanoparticles applied in biological milieu, the covered proteins corona will change the zeta potential of nanoparticles, Zhang et al. [38] found that with corona the zeta potential of all the nanoparticles they used changed from positive to negative. X-ray diffraction further demonstrated that these particles have distinct diffraction angles (2θ) (Fig. 1C), which matched with the characteristic phases of γ-Fe_2O_3 crystal as defined by the Joint Committee of Powder Diffraction Standards. Infrared (IR) spectrum analysis (Fig. 1D) indicated that particles had an absorbance at a range from 3300 cm^{-1} to 3500 cm^{-1}, corresponding to OH stretching vibration; two absorbances at 1610 cm^{-1} and 1457 cm^{-}, corresponding to COO– stretching vibration; and an absorbance at 583 cm^{-1}, corresponding to Fe_2O_3 stretching vibration. This spectrum is consistent with the characteristic structure of PSC-coated Fe_2O_3. Finally, we analyzed the magnetic hysteresis loop of MNPs and demonstrated that the particles were superparamagnetic as they had a saturation magnetization of 65 emu/g (Fig. 1E).

To evaluate the potential cytotoxicity of MNPs, we analyzed MNPs-treated macrophage RAW cells with MTT, a nonradioactive colorimetric assay that measures cell viability. Although there was a slight increase in cell viability at low concentrations of MNPs as compared with untreated cells (Fig. 1F), such increase was slightly declined when the concentration of MNPs was increased. Importantly, there was no significant difference in the viability between treated and untreated cells at all the tested concentrations, which ranged from 10 to 2500 μg/mL. Thus, the prepared MNPs had a high biocompatibility under the conditions used in this report.

To verify that the prepared MNPs were able to be internalized by cells, we used TEM to analyze RAW cells that had been treated with MNPs for 4 h. As shown in Fig. 2A, internalized MNPs were readily detected in the cytoplasm of treated cells as high electron densities. High magnification images (Fig. 2B and C) further indicated that internalized MNPs were accumulated in intracellular vesicles.

3.2. MIM promoted MNPs internalization

MIM is a cellular protein that is involved in endocytosis [39]. To analyze whether there was a functional relationship between MNPs internalization and MIM, we established stable RAW cells expressing either MIM-GFP or GFP. Internalization of MNPs in established cells was initially analyzed based on side scattering (SSC), the property that varies in the MNPs-mediated cellular granularity [35,40]. After 4 h treatment, RAW-MIM-GFP cells exhibited a greater increase in SSC, as measured by flow cytometry, than did RAW-GFP cells as indicated by larger rightward shifts along with increased MNPs (Fig. 3A and Fig. S1). To confirm the effect of MIM on MNPs internalization, we further analyzed cell-associated MNPs based on o-phenanthroline photometric analysis, which measured iron loads per milligram of proteins within cells. As shown in Fig. 3B, when compared to RAW-GFP cells, RAW-MIM-GFP cells showed slight but consistent increases in iron loads at all the concentrations examined. Especially, at the concentrations of 50 and 100 μg/mL, the increases were statistically significant. Finally, MIM-GFP expressing cells were examined by Prussian blue staining, which produced blue pigments when irons interacted with ferrous ferrocyanide. As shown in Fig. 3C, Prussian blue staining was positive only in the cells treated with MNPs. However, the staining intensity with RAW-MIM-GFP cells was greater than that with RAW-GFP cells (Fig. 3D).

Clathrin-mediated endocytosis is considered as the primary pathway for the uptake of nanoparticles including MNPs [18], [41,42]. It is known that certain clathrin-binding proteins are BAR domain proteins [43,44]. Therefore, we were interested in whether MIM could also influence MNPs uptake by interacting with clathrin. Mammalian clathrin contains two subunits: clathrin heavy chain (CHC) and clathrin light chain (CLC). In a previous study, we had demonstrated MIM was colocalized with CHC after 4 h of MNP treatment [31]. To determine whether MIM also interacted with CLC, RAW cells were co-stained with MIM and CLC antibodies conjugated with FITC and RBITC, respectively. Both antibodies produced distinct punctate staining patterns in the cytoplasm with little co-localization in untreated cells. However, after incubation with MNPs for 4 h, MIM was evidently co-localized with CLC (Fig. 4A). Quantitative analysis based on Mander's coefficient estimated that nearly 70% CLC was colocalized with MIM in treated cells whereas < 10% clathrin overlapped with MIM in untreated cells (Fig. 4B).

The interaction between MIM and each clathrin subunit was also examined by co-immunoprecipitation assay (Co-IP). In this assay, RAW cells were first treated with 100 μg/mL MNPs for times up to 240 min, the duration in which no change in the expression of either clathrin (both heavy and light chain) or MIM proteins had been observed (Fig. 5A). At different times after the treatment, the lysates of treated cells were precipitated with MIM antibodies, and the presence of clathrin subunits in the precipitates was analyzed by Western blot using their corresponding antibodies. As shown in Fig. 5A and B, CLC was readily co-precipitated with MIM in a time-dependent manner. Especially, the precipitation was greatly enhanced at an early phase (5 to 10 min) and a late phase (90 to 240 min) (Fig. 5B). In contrast, the interaction between MIM and CHC was barely detectable during this period except of 240 min, at which a modest interaction was observed (Fig. 5A). This data indicated that MIM may form a complex with CLC. To verify this, cell lysates derived from MNP-treated cells were also precipitated with antibodies against either CHC or CLC, and the presence of MIM in the precipitates was detected by Western blot using MIM antibody. This reversal Co-IP also showed that MIM interacted more readily with CLC than with CHC (Fig. 5C). This result was surprising as CLC is a component of clathrin triskelion, the backbone of clathrin lattice [45]. It is possible that MIM may participate in a function of CLC that is not involved in the formation of clathrin lattices during initial MNP endocytosis.

3.3. MIM promotes intracellular sorting of MNPs

As MNPs were accumulated in cytoplasmic vesicles after

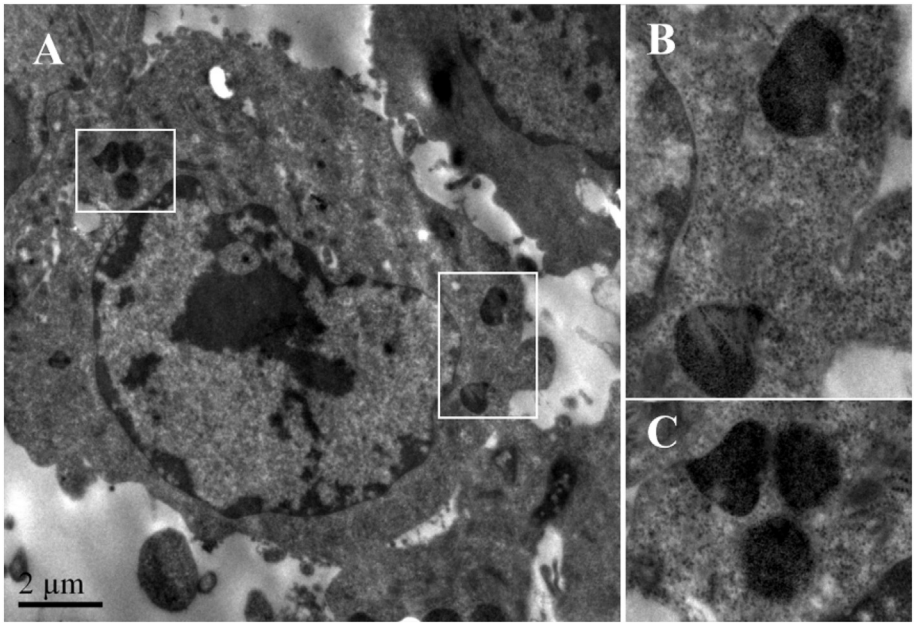

Fig. 2. Electron microscopic analysis of internalized MNPs. RAW cells were treated with 100 μg/mL MNPs for 4 h and processed for TEM. A representative image was provided (A). The boxed areas in image A were amplified on B and C, respectively, to show the details of internalized particles.

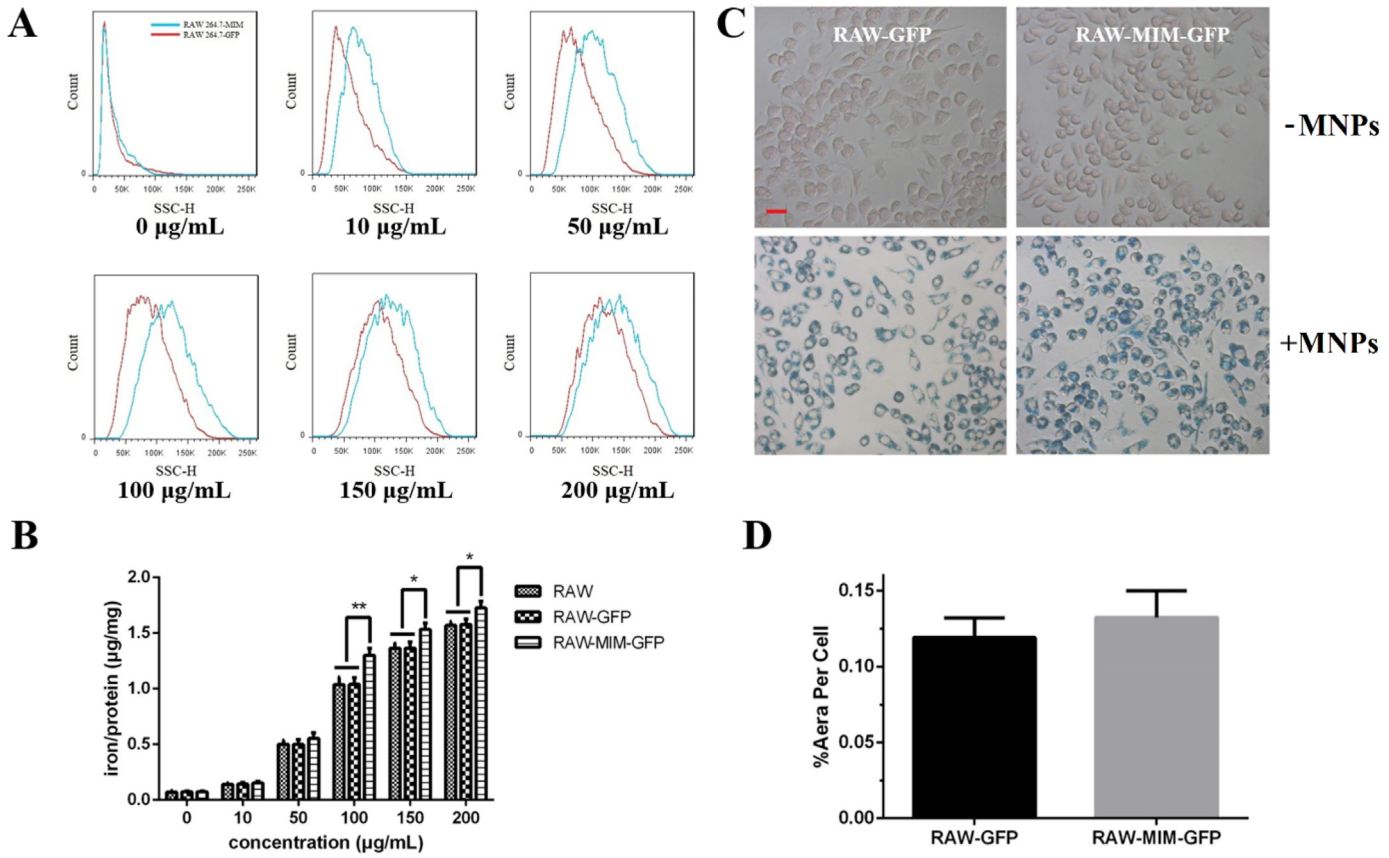

Fig. 3. Overexpression of MIM promoted MNPs internalization. (A) Flow cytometric analysis of side scattering of RAW-GFP and RAW-MIM-GFP cells after 4 h of treatment with MNPs at concentrations as indicated. (B) Analysis of MNP uptake based on iron loads. Cells were treated with MNPs for 24 h at concentrations as indicated. The iron loads of each sample were measured based on the formation of Fe-phenanthroline complex, which was quantified as described in the section of Material and Methods. The quantified iron loads were also normalized to the protein concentration. The data was presented as the mean ± SD. $^{*}P < .05$, $^{**}P < .01$. (C) RAW-GFP and RAW-MIM-GFP cells were treated or untreated with MNPs at 100 μg/mL. After 4 h, the cells were stained with Prussian blue and photographed under light microscope. Scale bar = 50 μm. (D) Prussian blue staining was quantitively analyzed by Image J software. The data shown represents mean ± SD of three independent experiments. In each experiment, 5 different microscopic areas were randomly chosen and analyzed.

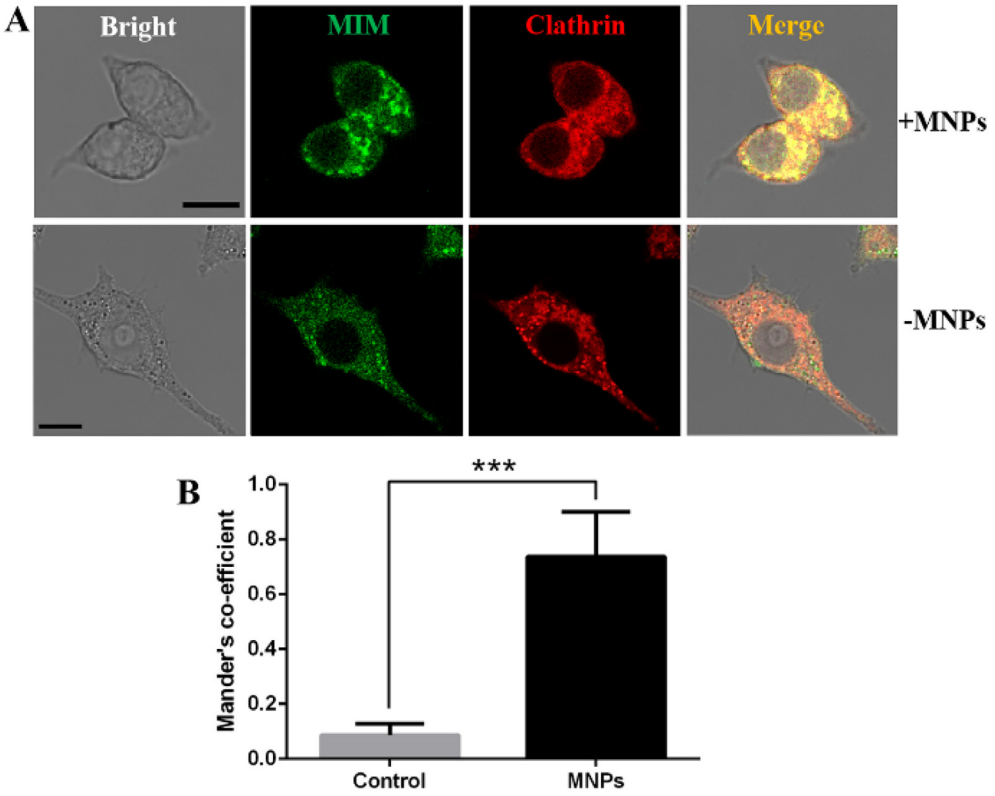

Fig. 4. MIM was co-localized with clathrin light chain. (A) RAW cells were incubated with 100 μg/mL MNPs for 4 h and co-stained with antibodies against MIM (green) and clathrin light chain (red). Scale bar = 10 μm. (B) Co-localization of MIM and CLC was quantitatively analyzed based on Mander's coefficient. All the data represent mean ± SD of three independent experiments. In each experiment, 50 cells were examined. ***, $P < .001$.

internalization (Fig. 2), it was possible that MIM promoted the uptake of MNPs by participating in intracellular trafficking of nanoparticles into endocytic vesicles once they were internalized. Indeed, MIM has been recently shown to bind small GTPases Rab5 and Rab7 in response to CXCL12, the ligand of CXCR4 [29]. To investigate whether these interactions were also implicated in endocytosis of MNPs, we examined by co-IP the association of MIM with Rab5 and Rab7 at different times after exposure to MNPs. As shown in Fig. 6A and B, although the interaction between MIM and Rab5 was readily detected prior to exposing to MNPs, it was nearly diminished at 5 min after MNPs treatment and slightly increased again in a late stage from 60 min to 240 min (Fig. 6C). In contrast, the interaction with Rab7 was barely detectable until 5 min and slightly reduced after 90 min. Thus, MIM was associated with Rab7 in a pattern that was apparently opposite to that with Rab5 (Fig. 6D).

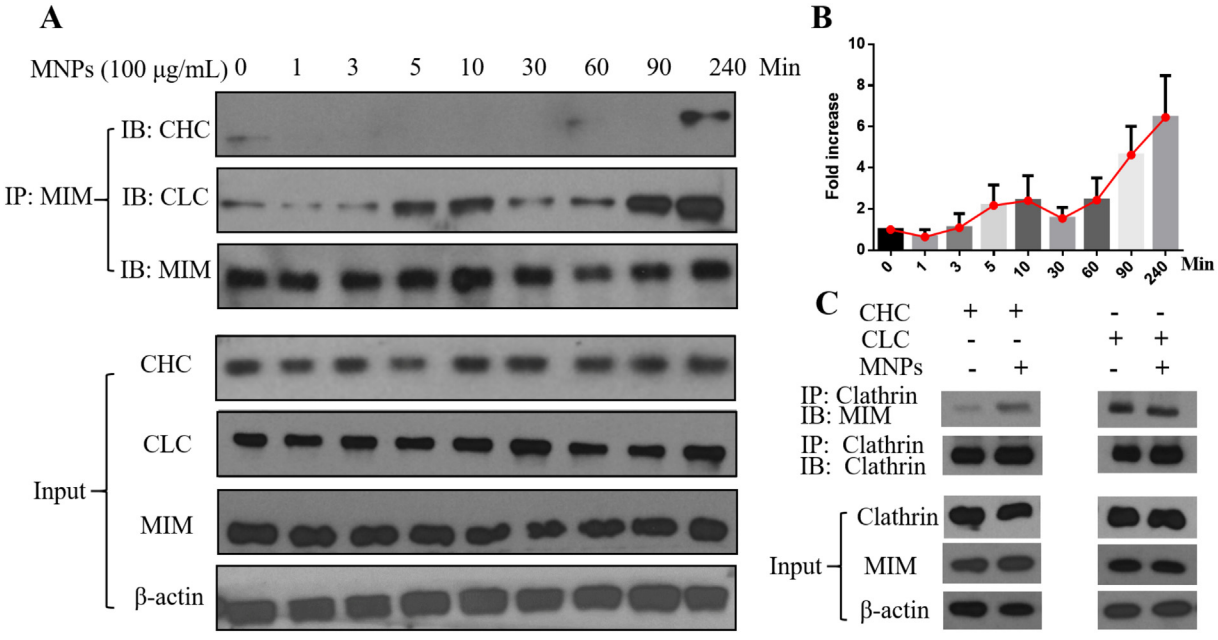

Fig. 5. MNPs promoted the interaction of MIM with clathrin light chain. (A) RAW cells were treated with 100 μg/mL MNPs for different times as indicated. The lysates of treated cells were analyzed by co-IP with MIM antibody followed by Western blot (IB) with antibodies as indicated. (B) Quantification of the amount of CLC detected by co-IP. (C) RAW cells were treated or untreated with 100 μg/mL MNPs for 4 h. The lysates of treated cells were immunoprecipitated by clathrin antibody and followed by Western blot using antibodies against different antigens as indicated.

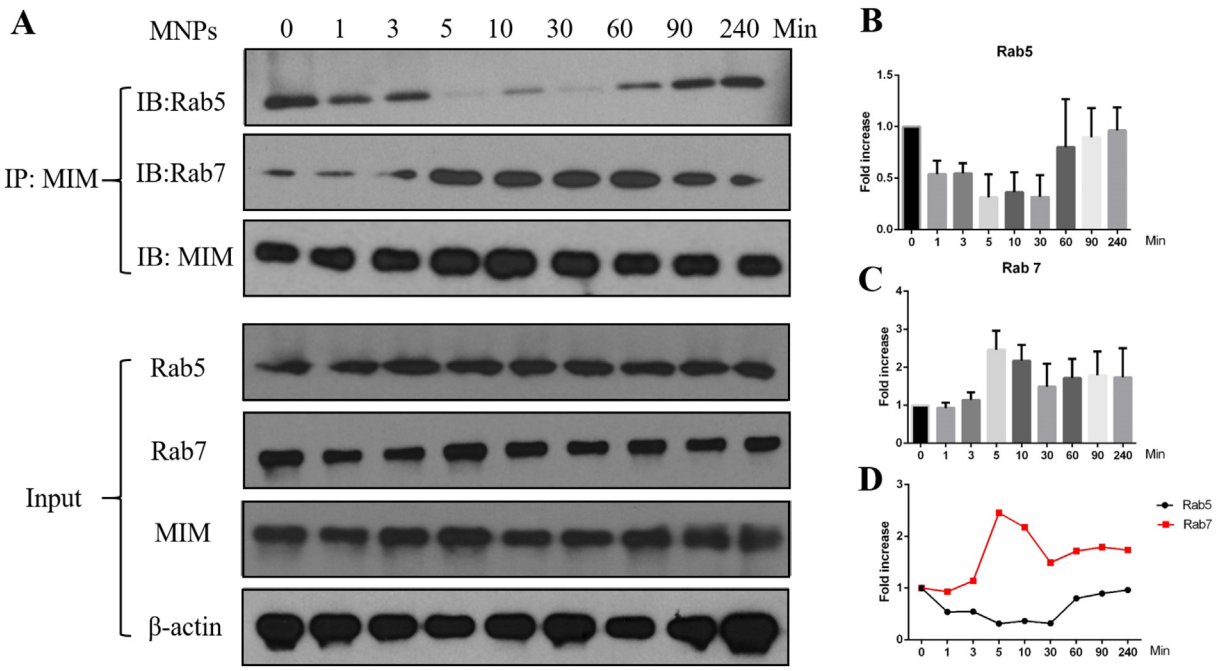

Fig. 6. MIM was associated differently with Rab5 and Rab7 in response to MNPs. (A) RAW cells were treated with 100 μg/mL of MNPs for the times as indicated. The treated cells were lysed and precipitated with MIM antibody followed by Western blot with antibodies against different antigens as indicated. (B and C) Quantification of the interaction between MIM and Rab5 (B) and Rab7 (C). All the data represent mean ± S.D. (n = 3). (D) Illustration of a reversed relationship in the binding of MIM to Rab5 and Rab7 based on the combination of the data of B and C.

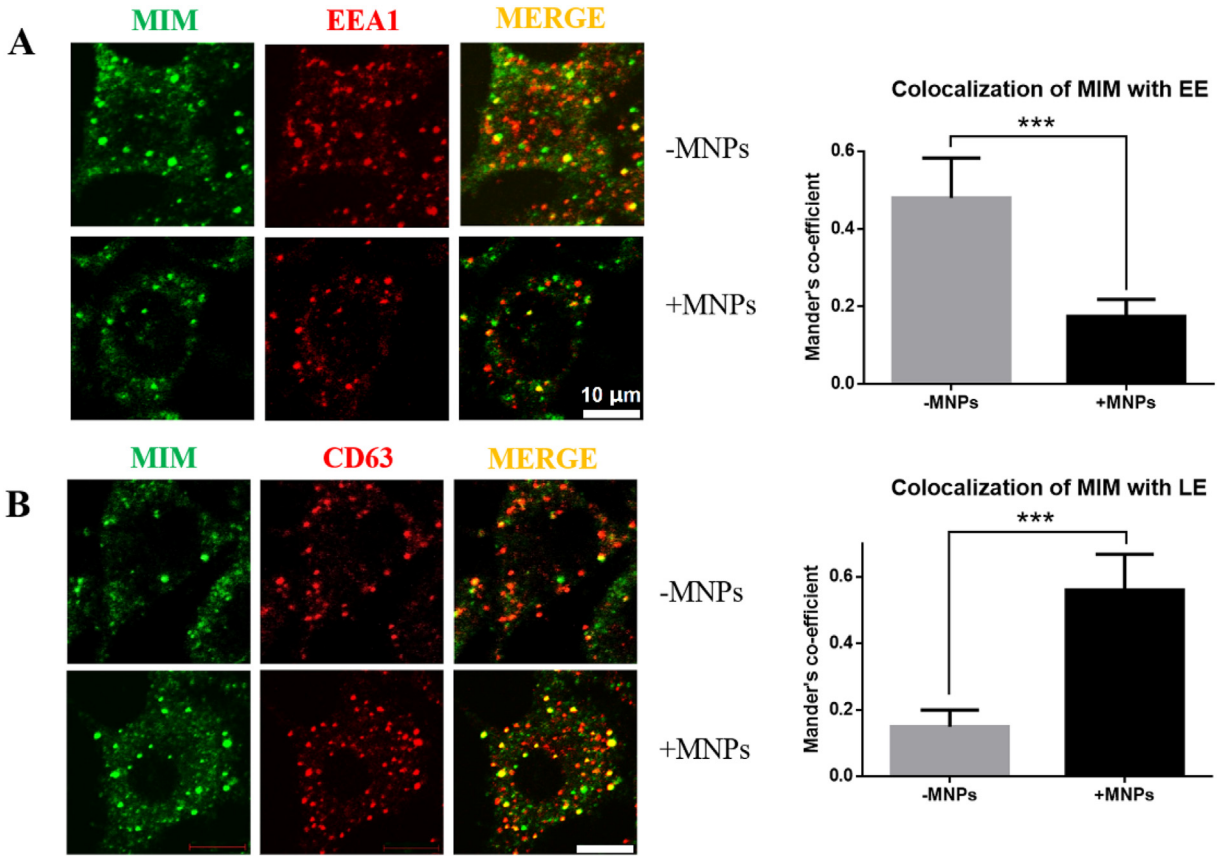

Fig. 7. MNPs promoted the association of MIM with late endosomes. RAW cells were treated or untreated with 100 μg/mL MNPs for 5 min. The treated cells were co-stained with MIM antibody (green) and EEA1 antibody (red) (A) or CD63 antibody (red) (B). The co-localization was estimated based on the Mander's coefficient. All the data represent mean ± SD of three independent experiments. In each experiment, 50 cells were examined. ***, P < .001.

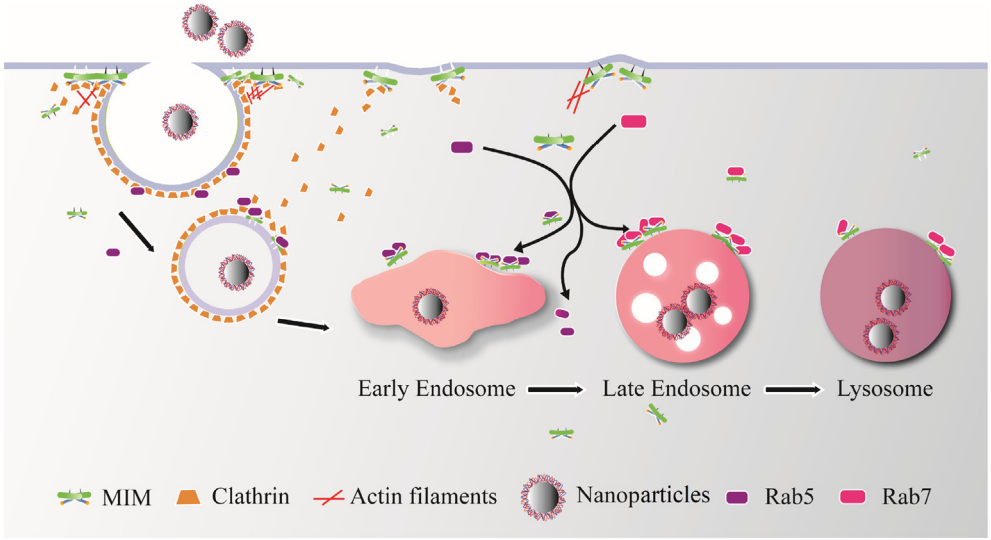

Fig. 8. Schematic illustration for MIM promotes internalization of magnetic nanoparticles *via* clathrin-mediated endocytosis and intracellular trafficking.

This inversed relationship suggests that MIM binds to Rab5 and Rab7 at the same site, resulting in their interactions exclusive to each other [29,46]. Notably, the interaction between MIM and CLC was also increased significantly at 5 min after MNPs treatment (Fig. 5A), consistent with the view that the MIM/CLC interaction may be involved in a phase of endocytosis that is temporally comparable with the association of MIM with Rab7, the enzyme that drives the transition from early endosomes to late endosomes [47].

To verify the function of MIM in early and late endosomes during the response to MNPs, we examined the colocalization of MIM with early endosomes as marked by EEA1 and late endosomes as marked by CD63 [48]. As shown in Fig. 7A, about 45% early endosomes were associated with MIM prior to MNPs treatment. After 5 min of treatment, colocalization of MIM and early endosomes was reduced to 18%. On the contrary, only 17% early endosomes were associated with MIM in non-treated cells; and 52% late endosomes were associated with MIM after 5 min of treatment (Fig. 7B). Consistent with a function of MIM in MNPs internalization during the transition from early endosomes to late endosomes, MNPs also induced a significant amount of MIM proteins sorted into lysosomes (Fig. S2).

4. Conclusions

In summary, we have provided evidence for the role of MIM in the intracellular trafficking of MNPs *via* interactions with CLC, Rab5 and Rab7. This finding is novel because this is the first report about the interaction between MIM and CLC in response to extracellular stimuli. Yet, at an early phase of internalization we did not find significant interaction between MIM CHC, which is known to be assembled into clathrin lattices in the initial uptake of cargos during receptor-mediated endocytosis. One explanation is that CLC has a function other than initiation of endocytosis. Indeed, it has been recently reported that CLC, but not CHC, is required for a rapid cycling of intracellular membrane to the cell surface from endosomes, a process that is driven by the actin polymerization [49]. Whether the interaction between MIM and CLC is involved in the formation of a specific type of membranes is unknown and worth to be further explored (Fig. 8).

Acknowledgements

This work was supported by NSFC Projects of International Cooperation and Exchanges No. (61420106012), the National Key Research and Development Program of China (No. 2017YFA0104302), Collaborative Innovation Center of Suzhou Nano Science and Technology, the Fundamental Research Funds for the Central Universities (No. 2242017 K40232). This research was also supported by National Cancer Institute (R01 CA113809 to X. Z.). We thank Dr. Hongyin Wang from the University of Texas Health Science Center for his assistance in confocal microscopy, and Dr. Xubo Lin from Beihang University for his assistance in Molecular Dynamics.

The authors declare no competing financial interest.

Appendix A. Supplementary data

Supplementary data to this article can be found online at https://doi.org/10.1016/j.bbagen.2018.12.002.

References

[1] V.F. Cardoso, A. Francesko, C. Ribeiro, M. Banobre-Lopez, P. Martins, S. Lanceros-Mendez, Advances in magnetic Nanoparticles for Biomedical applications, Adv Healthc Mater 7 (2018) 1700845.
[2] L. Chen, J. Xie, H.A. Wu, F.C. Zang, M. Ma, Z.C. Hua, N. Gu, Y. Zhang, Improving sensitivity of magnetic resonance imaging by using a dual-targeted magnetic iron oxide nanoprobe, Colloids and Surfaces B-Biointerfaces 161 (2018) 339–346.
[3] M. Ma, Y. Zhang, X.L. Shen, J. Xie, Y. Li, N. Gu, Targeted inductive heating of nanomagnets by a combination of alternating current (AC) and static magnetic fields, Nano Res. 8 (2015) 600–610.
[4] L. Li, W. Jiang, K. Luo, H.M. Song, F. Lan, Y. Wu, Z.W. Gu, Superparamagnetic Iron Oxide Nanoparticles as MRI contrast agents for Non-invasive Stem Cell labeling and Tracking, Theranostics 3 (2013) 595–615.
[5] J. Lee, M. Morita, K. Takemura, E.Y. Park, A multi-functional gold/iron-oxide nanoparticle-CNT hybrid nanomaterial as virus DNA sensing platform, Biosens. Bioelectron. 102 (2018) 425–431.
[6] F. Xiong, S. Huang, N. Gu, Magnetic nanoparticles: recent developments in drug delivery system, Drug Dev. Ind. Pharm. 44 (2018) 697–706.
[7] Y. Liu, F. Yang, C. Yuan, M. Li, T. Wang, B. Chen, J. Jin, P. Zhao, J. Tong, S. Luo, N. Gu, Magnetic Nanoliposomes as in Situ Microbubble Bombers for Multimodality Image-Guided Cancer Theranostics, ACS Nano 11 (2017) 1509–1519.
[8] B. Wang, X. He, Z.Y. Zhang, Y.L. Zhao, W.Y. Feng, Metabolism of Nanomaterials in Vivo: Blood Circulation and Organ Clearance, Acc. Chem. Res. 46 (2013) 761–769.
[9] M. Hadjidemetriou, K. Kostarelos, Nanomedicine: Evolution of the nanoparticle corona, Nat. Nanotechnol. 12 (2017) 288–290.
[10] A.E. Nel, L. Madler, D. Velegol, T. Xia, E.M.V. Hoek, P. Somasundaran, F. Klaessig, V. Castranova, M. Thompson, Understanding biophysicochemical interactions at the nano-bio interface, Nat. Mater. 8 (2009) 543–557.
[11] W. Xiao, J.Y. Xiong, S. Zhang, Y. Xiong, H.J. Zhang, H.L. Gao, Influence of ligands property and particle size of gold nanoparticles on the protein adsorption and corresponding targeting ability, Int. J. Pharm. 538 (2018) 105–111.
[12] E. Blanco, H. Shen, M. Ferrari, Principles of nanoparticle design for overcoming biological barriers to drug delivery, Nat. Biotechnol. 33 (2015) 941–951.
[13] S. Salatin, S.M. Dizaj, A.Y. Khosroushahi, Effect of the surface modification, size, and shape on cellular uptake of nanoparticles, Cell Biol. Int. 39 (2015) 881–890.
[14] W. Xiao, H. Gao, The impact of protein corona on the behavior and targeting capability of nanoparticle-based delivery system, Int. J. Pharm. 552 (2018)

328–339.
[15] L. Liu, T.K. Hitchens, Q. Ye, Y. Wu, B. Barbe, D.E. Prior, W.F. Li, F.C. Yeh, L.M. Foley, D.J. Bain, C. Ho, Decreased reticuloendothelial system clearance and increased blood half-life and immune cell labeling for nano- and micron-sized superparamagnetic iron-oxide particles upon pre-treatment with Intralipid, Biochim. Biophys. Acta 1830 (2013) 3447–3453.
[16] E. Allard-Vannier, K. Herve-Aubert, K. Kaaki, T. Blondy, A. Shebanova, K.V. Shaitan, A.A. Ignatova, M.L. Saboungi, A.V. Feofanov, I. Chourpa, Folic acid-capped PEGylated magnetic nanoparticles enter cancer cells mostly via clathrin-dependent endocytosis, Biochim. Biophys. Acta Gen. Subj. 1861 (2017) 1578–1586.
[17] S. Mayor, R.E. Pagano, Pathways of clathrin-independent endocytosis, Nat. Rev. Mol. Cell Biol. 8 (2007) 603–612.
[18] C.Y. Yang, M.F. Tai, C.P. Lin, C.W. Lu, J.L. Wang, J.K. Hsiao, H.M. Liu, Mechanism of Cellular Uptake and Impact of Ferucarbotran on Macrophage Physiology, PLoS One 6 (2011) e25524.
[19] L. Li, H. Liu, S.S. Baxter, N. Gu, M. Ji, X. Zhan, The SH3 domain distinguishes the role of I-BAR proteins IRTKS and MIM in chemotactic response to serum, Biochem. Biophys. Res. Commun. 479 (2016) 787–792.
[20] X. Lin, H. Wang, Z. Lou, M. Cao, Z. Zhang, N. Gu, Roles of PIP2 in the membrane binding of MIM I-BAR: insights from molecular dynamics simulations, FEBS Lett. 592 (15) (2018) 2533–2542.
[21] R. Lundmark, S.R. Carlsson, Driving membrane curvature in clathrin-dependent and clathrin-independent endocytosis, Semin. Cell Dev. Biol. 21 (2010) 363–370.
[22] M. Meinecke, E. Boucrot, G. Camdere, W.C. Hon, R. Mittal, H.T. McMahon, Cooperative recruitment of dynamin and BIN/amphiphysin/Rvs (BAR) domain-containing proteins leads to GTP-dependent membrane scission, J. Biol. Chem. 288 (2013) 6651–6661.
[23] M. Wu, B. Huang, M. Graham, A. Raimondi, J.E. Heuser, X. Zhuang, P. De Camilli, Coupling between clathrin-dependent endocytic budding and F-BAR-dependent tubulation in a cell-free system, Nat. Cell Biol. 12 (2010) 902–908.
[24] S.M. Ferguson, A. Raimondi, S. Paradise, H. Shen, K. Mesaki, A. Ferguson, O. Destaing, G. Ko, J. Takasaki, O. Cremona, O.T. E, P. De Camilli, Coordinated actions of actin and BAR proteins upstream of dynamin at endocytic clathrin-coated pits, Dev. Cell, 17 (2009) 811–822.
[25] T. Zhan, C. Cao, L. Li, N. Gu, C.I. Civin, X. Zhan, MIM regulates the trafficking of bone marrow cells via modulating surface expression of CXCR4, Leukemia 30 (2016) 1327–1334.
[26] D.M. Veltman, G. Auciello, H.J. Spence, L.M. Machesky, J.Z. Rappoport, R.H. Insall, Functional analysis of Dictyostelium IBARa reveals a conserved role of the I-BAR domain in endocytosis, Biochem. J. 436 (2011) 45–52.
[27] K.D. Mertz, G. Pathria, C. Wagner, J. Saarikangas, A. Sboner, J. Romanov, M. Gschaider, F. Lenz, F. Neumann, W. Schreiner, M. Nemethova, A. Glassmann, P. Lappalainen, G. Stingl, J.V. Small, D. Fink, L. Chin, S.N. Wagner, MTSS1 is a metastasis driver in a subset of human melanomas, Nat. Commun. 5 (2014) 3465.
[28] G.A. Quinones, J. Jin, A.E. Oro, I-BAR protein antagonism of endocytosis mediates directional sensing during guided cell migration, J. Cell Biol. 189 (2010) 353–367.
[29] L. Li, S.S. Baxter, N. Gu, M. Ji, X. Zhan, Missing-in-metastasis protein downregulates CXCR4 by promoting ubiquitylation and interaction with small Rab GTPases, J. Cell Sci. 130 (2017) 1475–1485.
[30] D. Yu, X.H. Zhan, X.F. Zhao, M.S. Williams, G.B. Carey, E. Smith, D. Scott, J. Zhu, Y. Guo, S. Cherukuri, C.I. Civin, X. Zhan, Mice deficient in MIM expression are predisposed to lymphomagenesis, Oncogene 31 (2012) 3561–3568.
[31] P. Zhao, M. Cao, L.N. Song, H. Wu, K. Hu, B. Chen, Q.W. Wang, N. Gu, Downregulation of MIM protein inhibits the cellular endocytosis process of magnetic nanoparticles in macrophages, RSC Adv. 6 (2016) 96635–96643.
[32] B. Chen, J. Sun, F. Fan, X. Zhang, Z. Qin, P. Wang, Y. Li, X. Zhang, F. Liu, Y. Liu, M. Ji, N. Gu, Ferumoxytol of ultrahigh magnetization produced by hydrocooling and magnetically internal heating coprecipitation, Nanoscale 10 (2018) 7369–7376.
[33] Y. Wang, K. Zhou, X.C. Zeng, J.X. Lin, X. Zhan, Tyrosine phosphorylation of missing in metastasis protein in implicated in platelet-derived growth factor-mediated cell shape changes, J. Biol. Chem. 282 (2007) 7624–7631.
[34] N. Nitin, L.E.W. Laconte, O. Zurkiya, X. Hu, G. Bao, Functionalization and peptide-based delivery of magnetic nanoparticles as an intracellular MRI contrast agent, J. Biol. Inorg. Chem. 9 (2004) 706–712.
[35] M.S. Lord, M. Jung, W.Y. Teoh, C. Gunawan, J.A. Vassie, R. Amal, J.M. Whitelock, Cellular uptake and reactive oxygen species modulation of cerium oxide nanoparticles in human monocyte cell line U937, Biomaterials 33 (2012) 7915–7924.
[36] B. Chen, Y. Li, X.Q. Zhang, F. Liu, Y.L. Liu, M. Ji, F. Xiong, N. Gu, An efficient synthesis of ferumoxytol induced by alternating-current magnetic field, Mater. Lett. 170 (2016) 93–96.
[37] X.B. Lin, Y. Li, N. Gu, Nanoparticle's size effect on its Translocation across a Lipid Bilayer: a Molecular Dynamics simulation, J Comput Theor Nanos 7 (2010) 269–276.
[38] H.J. Zhang, T.M. Wu, W.Q. Yu, S.B. Ruan, Q. He, H. Gao, Ligand size and Conformation Affect the Behavior of Nanoparticles Coated with in Vitro and in Vivo Protein Corona, ACS Appl. Mater. Interfaces 10 (2018) 9094–9103.
[39] M. Cao, T.L. Zhan, M. Ji, X. Zhan, Dimerization is necessary for MIM-mediated membrane deformation and endocytosis, Biochem. J. 446 (2012) 469–475.
[40] M. Wang, M. Cao, Z.R. Guo, N. Gu, Generalized multiparticle Mie modeling of light scattering by cells, Chin. Sci. Bull. 58 (2013) 2663–2666.
[41] H. Herd, N. Daum, A.T. Jones, H. Huwer, H. Ghandehari, C.M. Lehr, Nanoparticle geometry and surface orientation influence mode of cellular uptake, ACS Nano 7 (2013) 1961–1973.
[42] A. Anas, T. Okuda, N. Kawashima, K. Nakayama, T. Itoh, M. Ishikawa, V. Biju, Clathrin-mediated endocytosis of quantum dot-peptide conjugates in living cells, ACS Nano 3 (2009) 2419–2429.
[43] H. Gad, N. Ringstad, P. Low, O. Kjaerulff, J. Gustafsson, M. Wenk, G. Di Paolo, Y. Nemoto, J. Crun, M.H. Ellisman, P. De Camilli, O. Shupliakov, L. Brodin, Fission and uncoating of synaptic clathrin-coated vesicles are perturbed by disruption of interactions with the SH3 domain of endophilin, Neuron 27 (2000) 301–312.
[44] S. Boulakirba, E. Macia, M. Partisani, S. Lacas-Gervais, F. Brau, F. Luton, M. Franco, Arf6 exchange factor EFA6 and endophilin directly interact at the plasma membrane to control clathrin-mediated endocytosis, Proc. Natl. Acad. Sci. U. S. A. 111 (2014) 9473–9478.
[45] T. Kirchhausen, Imaging endocytic clathrin structures in living cells, Trends Cell Biol. 19 (2009) 596–605.
[46] A. Wandinger-Ness, M. Zerial, Rab proteins and the compartmentalization of the endosomal system, Cold Spring Harb. Perspect. Biol. 6 (2014) a022616.
[47] P. Sandin, L.W. Fitzpatrick, J.C. Simpson, K.A. Dawson, High-speed imaging of Rab family small GTPases reveals rare events in nanoparticle trafficking in living cells, ACS Nano 6 (2012) 1513–1521.
[48] R. Ghossoub, F. Lembo, A. Rubio, C.B. Gaillard, J. Bouchet, N. Vitale, J. Slavik, M. Machala, P. Zimmermann, Syntenin-ALIX exosome biogenesis and budding into multivesicular bodies are controlled by ARF6 and PLD2, Nat. Commun. 5 (2014).
[49] S.R. Majeed, L. Vasudevan, C.Y. Chen, Y. Luo, J.A. Torres, T.M. Evans, A. Sharkey, A.B. Foraker, N.M. Wong, C. Esk, T.A. Freeman, A. Moffett, J.H. Keen, F.M. Brodsky, Clathrin light chains are required for the gyrating-clathrin recycling pathway and thereby promote cell migration, Nat. Commun. 5 (2014) 3891.